Design of low-voltage integrated step-up oscillators with microtransformers for energy harvesting applications

Published Version:
Enrico Macrelli,
Aldo Romani,
Rudi Paolo Paganelli,
Antonio Camarda,
Marco Tartagni (2015). Design of low-voltage integrated step-up oscillators with microtransformers for energy harvesting applications. IEEE TRANSACTIONS ON CIRCUITS AND SYSTEMS. I, REGULAR PAPERS, 62(7), 1747-1756 [10.1109/TCSI.2015.2423796].

Availability:

This version is available at: https://hdl.handle.net/11585/456569 since: 2015-09-10

Published:

DOI: http://doi.org/10.1109/TCSI.2015.2423796

Design of Low-Voltage Integrated Step-up Oscillators with Microtransformers for Energy Harvesting Applications

Enrico Macrelli, Aldo Romani, Rudi Paolo Paganelli, Antonio Camarda, and Marco Tartagni, *Member, IEEE*

***Abstract*—This paper describes the modeling of startup circuits in battery-less micropower energy harvesting systems and investigates the use of bond wire micromagnetics. The analysis focuses on step-up Meissner oscillators based on magnetic core transformers operating with input voltages down to ≈100 mV, e.g. from thermoelectric generators. As a key point, this paper examines the effect of core losses and leakage inductances on the startup requirements obtained with the classical Barkhausen criterion, and demonstrates the minimum transconductance for oscillations to occur. For validation purposes, a step-up oscillator IC is fabricated in a STMicroelectronics 0.32 µm technology, and connected to two bond wire microtransformers, respectively, with a 1:38 MnZn ferrite core and with a 1:52 ferromagnetic low-temperature co-fired ceramic (LTCC) core. Coherently with the proposed model, experimental measurements show a minimum startup voltage of 228 mV for the MnZn ferrite core and of 104 mV for the LTCC core.**

***Index Terms*—Bond wire magnetics, energy harvesting, integrated circuits, leakage inductances, magnetic losses, magnetic materials, step-up oscillators, transformers.**

I. Introduction

In energy harvesting (EH) applications, several types of energy transducers are used to convert environmental energy into electrical form [1]. Such energy is then managed to supply low-power and low-voltage circuits. Battery-powered systems are widespread in miniaturized electronics; however, batteries are not suitable for wireless sensor nodes (WSNs) or bio-implantable systems where periodic maintenance is difficult. For these applications, EH is the best choice for long-lasting power production and low maintenance. Among the available types of energy transducers, thermoelectric generators (TEGs) may provide sufficient power for sustaining battery-less WSNs and, in general, for supplying fully autonomous systems. TEGs consist of arrays of thermocouples containing a p-type and n-type semiconductor connected electrically in series and thermally in parallel. Because of the Seebeck effect, the output voltage of a TEG is proportional to the number of thermocouples and to the temperature difference between cold and hot side [2]. TEGs with voltage outputs from 10 to 50 mV/K have been fabricated with microelectronic processes [3] with low series resistances typically lower than 1 Ω. For body-wearable applications, a temperature gradient of 5 K between body and environment is expected to generate an output voltage lower than 250 mV.

Under these conditions, when no initial energy is available, particular ultralow voltage step-up converters are required in order to kick-start battery-less systems from fully discharged states. Since in standard CMOS technologies the usual threshold voltage of a MOSFET is in the order of few hundreds of mV, self-starting designs from lower voltages would require a normally-ON device [4] [5] to allow current to circulate at the beginning. These circuits would then produce higher output voltages appropriate for standard CMOS circuits, so that a conventional power converter can be started and operated efficiently [6] [7]. We point out that the main design goal is to achieve the lowest possible activation voltage, rather than optimum efficiency, which will be guaranteed once the conventional power converter is started.

In the current state-of-the-art, several architectures of low-voltage step-up converters are implemented using TEGs. In [8] [9] various step-up converters based on a FET-tuned oscillator topology are reported. However, the startup of these circuits generally relies on a step-up transformer and a normally-ON MOSFET with a high ON-resistance, typically a few Ω, compared to the source resistance, that restricts the achievable output power [5]. A first solution to overcome this problem is the realization of the startup circuit separated from the main power conversion block, so that classical high efficiency dc-dc converters can be used. Charge pumps are a common implementation of this approach [4], [10]-[12], but alternative solutions relying on mechanical vibrations have also been developed [13]. A second solution is to merge the startup circuit with the main dc-dc converter in order to decrease the number of devices and to improve the reliability. Synchronous and flyback boost converters are examples of

This research was founded in part by the European Community's FP7 2007-2013 under grant agreement Nanofunction no. 257375 and by the ENIAC-JTI under grant agreement LAB4MEMS no. 325622.

E. Macrelli at the time of submission was with the Department of Electrical, Electronic, and Information Engineering, University of Bologna, Cesena I-47521, Italy. He is now with the Department of Electrical and Computer Engineering, National University of Singapore, Singapore 117583 (e-mail: enrico.macrelli@nus.edu.sg).

A. Romani, A. Camarda, and M. Tartagni are with the Department of Electrical, Electronic, and Information Engineering, University of Bologna, Cesena I-47521, Italy (e-mail: aldo.romani@unibo.it; antonio.camarda@unibo.it; marco.tartagni@unibo.it).

R. P. Paganelli is with the National Research Council CNR-IEIIT, c/o University of Bologna, Bologna I-40136, Italy (e-mail: rudipaolo.paganelli@cnr.it).

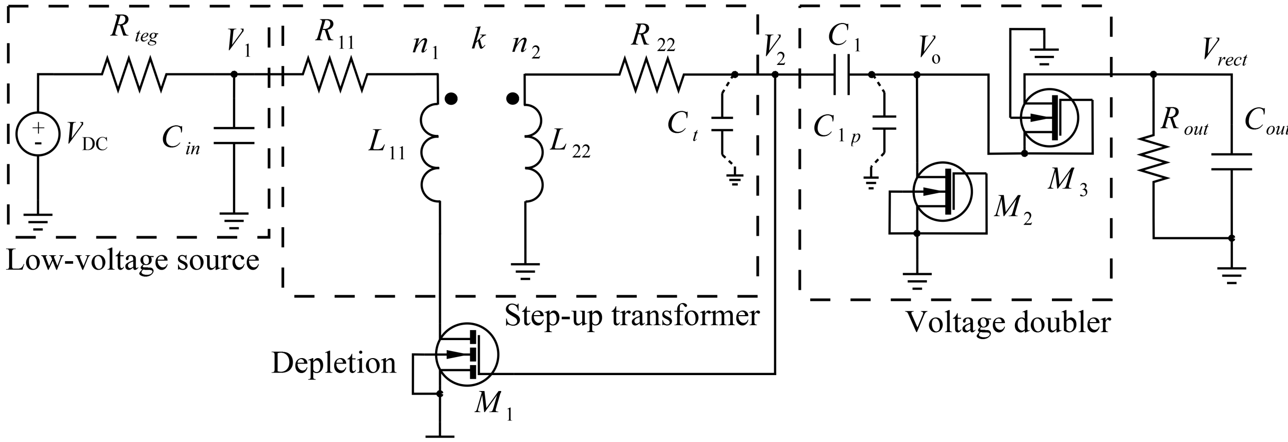

Fig. 1. Schematic of the designed low-voltage step-up oscillator with a step-up transformer. Parasitic capacitances are also included.

merged architectures as in [14], where 0.6 V are required for the startup along with several off-chip components. Other examples of merged architectures are step-up oscillators based on transformers or cross-coupled inductors as in [5], [15]-[17]. Recently, several circuits operating at low-voltages have been reported in literature [18]-[26], and as commercial products [27] [28].

Toroidal micromagnetics are considered one of the best choices for implementing step-up oscillators based on transformers due to the good dc performance within a small footprint area. Nowadays, commercial miniature transformers for EH are available with high inductance and high turns ratio [29] [30], however with: (i) high dc resistance, i.e. 200 Ω at secondary for 1 : 50 turns, (ii) large dimensions, i.e. $6.0 \times 6.0 \times 3.5$ mm^3 ($l \times w \times h$), (iii) high profile compared to micro-structures [31]. Besides this, literature reports toroidal microtransformers with bonding wires [32]-[34] with high quality-factor Q, small area and high turns ratio, which are features of paramount importance for low-voltage step-up oscillators [27]. The use of bonding wires allows in perspective die-level or in-package integration of the whole converter with the magnetics mounted on-top of the IC. In [32] and [33], transformers with NiZn and MnZn ferrite cores on a PCB substrate are reported with a turns ratio up to 1:38, a self-inductance up to 315 μH, and a small-signal peak Q-factor up to 24.5 at 0.1 MHz. In [34], a 29 μH 1:50 transformer is described with a ferromagnetic low-temperature co-fired ceramic (LTCC) core on silicon, with a peak Q-factor of 11.6 at 1.3 MHz, and a maximum primary current of ≈1 A.

II. Description of Work

An ideal transformer virtually presents zero winding and core losses, and unity coefficient of coupling. However, toroidal micromagnetics can exhibit large core losses due to eddy currents and hysteresis for increasing operating frequencies, depending on the core properties. In addition, these devices can experience lower coupling factors due to leakage inductances, depending on the winding structure and geometry, and on the core material. Both of these factors critically impact the performance of the step-up converter by increasing the minimum startup voltage. Currently, there is poor literature regarding this topic, thus it is very helpful to analyze the effect of core losses and leakage inductances on the startup requirements in order to better design low-voltage step-up circuits in EH applications.

This paper presents the design of a step-up oscillator circuit acting as a voltage booster from discharged states for use in battery-less systems, and suitable for operation with low-voltage sources such as TEGs. The circuit also takes advantage of miniaturized bond wire transformers with magnetic cores. The proposed circuit analysis includes the effects of core losses and leakage inductances on the startup requirements, and identifies the minimum active device transconductance necessary for oscillations to occur with a potential lossy and loosely coupled microtransformer. Additionally, given a specific transformer, circuit parameters can be optimized, and the minimum requirements can be found. Similarly, if circuit parameters are constrained, the model contributes to define the requirements of the magnetic component, thus allowing to explore the design space. Experimental results obtained with two bond wire transformers with ferrite and magnetic LTCC cores validate circuit analysis by confirming the low-voltage startup capability of the designed oscillator circuit.

The paper is structured as follows. Section III introduces a circuital analysis of low-voltage step-up oscillators for EH and recalls the main properties of the used bond wire microtransformers. Section IV discusses the modeling results together with the experimental results. Finally, the conclusions are presented in Section V.

III. Low-Voltage Step-Up Oscillator for Energy Harvesting Applications

This section presents the large and the small-signal analyses of the step-up converter. The analytical study also evaluates the startup capability of the converter and predicts the minimum transconductance which permits oscillations. Finally, the properties of the bond wire microtransformers used during validation are summarized.

A. Circuit Description

The designed step-up converter is based on a FET-tuned oscillator similar to that described in [18] and [27] with self-startup capability from very low voltage. The circuit relies on a Meissner-type oscillator, a modified version of the standard

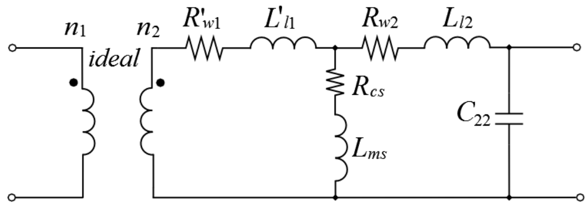

Fig. 2. Exact equivalent circuit of the step-up transformer referred at the secondary side with core losses and leakage inductances.

Hartley-type oscillator [26] [35]. Fig. 1 shows the schematic of the low-voltage step-up converter. The oscillator is composed of the step-up transformer and a depletion n-type MOSFET. A voltage doubler is also included. An integrated circuit (IC) including the MOSFET and the voltage doubler is realized in a STMicroelectronics 0.32 µm technology.

The energy source is modeled with a dc voltage $V_{DC} = V_{teg}$ and a series resistor R_{teg}, chosen to match the properties of a CP14 module from Laird Technologies [36]. The depletion n-type MOSFET M_1 is chosen due to its normally-ON state at the considered low voltages because of its negative threshold voltage V_{tn1}. The step-up transformer has a toroidal structure with n_1 turns at the primary coil and n_2 turns at the secondary coil. The transformer model shown in Fig. 1 includes [37]: the coupling coefficient k, the self-inductances L_{11} and L_{22}, the series resistances R_{11} and R_{22}, and the turns ratio $n_{12} = n_2 / n_1$. Besides, several capacitances are included in the analysis. The total capacitance is $C_t = C_{22} + C_{gs1} + C_{par}$, where C_{22} is the secondary parasitic capacitance of the transformer, C_{gs1} is the gate-source capacitance of M_1, and C_{par} is the total parasitic capacitance of IC pads and oscilloscope probes. C_1 is an integrated poly-poly capacitor, with an associated additional parasitic capacitance C_{1p} between its minus terminal and ground, whereas we neglect the parasitic capacitance between its plus terminal and ground and the capacitance between the coils. An external filter capacitor C_{in} acts as energy buffer.

B. Circuit Analysis

The circuit analysis presented herein is generic and independent on the chosen microelectronic process. Initially, the converter is connected to the energy source V_{DC} that imposes the current I_1 through the primary winding and the normally-ON depletion MOSFET. Hence, this current induces a positive voltage V_2 at the secondary coil ($V_2 > 0$ V) which increases the gate-source voltage $V_{gs1} = V_2$ of M_1 and thus I_1. Once I_1 reaches the core saturation, the voltage V_2 starts to drop, which lowers the drain current I_1, thus decreasing again V_2 below zero, by a loop until M_1 is driven near its off-state ($V_2 < 0$ V) leading to $I_1 \approx 0$. Preliminary current is delivered by the weak-inverted M_1, thus providing an increase of I_1, and thus, through the coupling of the coils, a further increase in V_2 causing M_1 to become more conductive again ($V_2 \approx 0$ V), so that the oscillation process starts [5]. The depletion-mode n-type MOSFET acts as a controlled resistor switched between the ON-state (low ON-resistance) and OFF-state (high ON-resistance), which modulates the current I_1. The last stage is a voltage doubler composed by the pump capacitor C_1 and the two diode-connected n-type enhancement MOSFETs M_2 and M_3. Finally, the load is composed of a storage capacitor C_{out} and a resistor R_{out}.

The behavior of the converter in Fig. 1 is influenced by the step-up transformer's performance such as coupling, winding resistances and core losses. In order to assess the oscillation mechanism at small-signals, the transformer's parameters are referred at the secondary side. The series resistances R_{11} and R_{22} are expressed as:

$$\begin{aligned} R_{11} &= R_{w1} + R_c \\ R_{22} &= R_{w2} + R_{cs}, \end{aligned} \tag{1}$$

where R_c is the core equivalent series resistance (ESR) and $R_{cs} = R_c\, n_{12}^2$ is the core ESR at secondary, whereas R_{w1} and R_{w2} are the winding resistances. The self-inductances L_{11} and L_{22} are expressed as:

$$\begin{aligned} L_{11} &= L_{l1} + L_m \\ L_{22} &= L_{l2} + L_{ms}, \end{aligned} \tag{2}$$

where L_{l1} and L_{l2} are the leakage inductances at primary and secondary, and L_m and L_{ms} are, respectively, the magnetizing inductances at primary and secondary. The latter quantities can be expressed as:

$$\begin{aligned} L_m &= k\, L_{11} \\ L_{ms} &= k\, L_{22} = L_m n_{12}^2. \end{aligned} \tag{3}$$

It descends from (2) and (3) that:

$$\begin{aligned} L_{l1} &= L_{11}(1-k) = L_m(1-k)/k \\ L_{l2} &= L_{22}(1-k) = L_{ms}(1-k)/k. \end{aligned} \tag{4}$$

Fig. 2 shows the exact equivalent circuit of the step-up transformer reported at the secondary side where:

$$\begin{aligned} R'_{w1} &= R_{w1}\, n_{12}^2 \\ L'_{l1} &= L_{l1}\, n_{12}^2 \approx L_{l2}, \end{aligned} \tag{5}$$

obtained by reporting the parameters at the secondary.

Let us now recall that V_{tn1} and V_{teg} are, respectively, the negative threshold voltage of the MOSFET M_1 and the open-circuit voltage of the TEG. From Fig. 1, since M_1 is connected in series with the primary coil, the drain-source voltage V_{ds1} has small values compared to V_{gs1} - V_{tn1}, thus forcing M_1 to operate always in triode mode (linear region) as a controlled resistor for low values of the source voltage V_{teg}. The drain current I_{ds1} in linear region is defined as:

$$I_{ds1} = \beta_{n1}\left(V_{gs1} - V_{tn1} - \frac{V_{ds1}}{2}\right)V_{ds1}, \tag{6}$$

where $\beta_{n1} = \mu_n\, C_{ox}\, W_1 / L$ is the gain factor of M_1, μ_n is the electron mobility, W_1 / L is the form factor of M_1, $C_{ox} = \varepsilon_{ox} / t_{ox}$ is the gate-oxide capacitance per unit area, with $\varepsilon_{ox} = \varepsilon_0\, \varepsilon_r$, $\varepsilon_r = 3.9$ for silicon dioxide, and t_{ox} as the gate-oxide thickness. In triode mode, the gate-to-channel capacitance of M_1 is due to the equal gate-source and gate-drain capacitances, which can be assumed to be in parallel under the assumption that V_{ds1} is small, as is the case in this application. Then, the overall capacitance is $C_{gs1} = C_{ox}\, W_1\, L$.

The transconductance g_{m1} of M_1 is computed from (6):

$$g_{m1} = \beta_{n1} V_{ds1} \approx \beta_{n1} \frac{V_{teg}}{1 - R_{eq}\beta_{n1}V_{tn1}}, \tag{7}$$

where $R_{eq} = R_{teg} + R_{11} + R_{con1}$, with R_{con1} as the parasitic resistance of connections at primary. The approximation in (7) is obtained for $V_{gs1} \approx 0$ by considering the DC voltage across L_{11} negligible, and by neglecting the quadratic term V_{ds1}^2 in (6) considering that $|V_{tn1}| >> V_{ds1}/2$ since we target ultra-low voltages of tens of mV. In order to maximize g_{m1}, V_{teg} together with β_{n1} should be increased, whereas R_{eq} and $|V_{tn1}|$ should be reduced. The output conductance g_{ds1} of M_1 is computed from (6):

$$g_{ds1} = \beta_{n1}(V_{gs1} - V_{tn1} - V_{ds1}) \approx \beta_{n1} \frac{R_{eq}\beta_{n1}V_{tn1}^2 - V_{teg} - V_{tn1}}{1 - R_{eq}\beta_{n1}V_{tn1}}, \quad (8)$$

where the same approximations of (7) hold. The ON-resistance of M_1 is $r_{ds} = 1 / g_{ds1}$, and can be referred to the secondary as $r'_{ds} = r_{ds}\, n_{12}^2$. Fig. 3 shows the resulting small-signal circuit. The total primary resistance referred at the secondary is $R'_{wt1} = (R_{teg} + R_{w1} + R_{con1})\, n_{12}^2$, whereas the total secondary resistance is $R_{wt2} = R_{w2} + R_{con2}$, with R_{con2} as the parasitic resistance of connections at secondary. From Fig. 3, the equivalent capacitance at secondary is $C_{eq} = C_t + (C_1 C_{1p}) / (C_1 + C_{1p})$.

The startup requirements are calculated by the Barkhausen criterion, which implies that the loop gain $A(f_0)\,\beta(f_0)$ at the oscillation frequency f_0, must be greater than unity, i.e. $A(f_0)\,\beta(f_0) \geq 1$, for oscillations to occur [35]. In this context, $A(f_0)$ represents the transconductance of M_1 seen from the secondary, while $\beta(f_0)$ is the transfer function of the linear feedback network. This further means that the magnitude of $A\beta$ must be greater than unity, i.e. $|A(f_0)\,\beta(f_0)| \geq 1$, while its phase shift must be equal to 0° or a multiple of 360°, i.e. $\arg(A(f_0)\,\beta(f_0)) = 0°$. Since the current over the secondary winding is $I_2 \cong I_1 / n_{12}$, we observe from Fig. 3 that $I_1 \cong g_{m1} V_{gs1}$, thus $I_2 \cong (g_{m1} V_{gs1}) / n_{12}$. In order to extract the startup condition we can open the loop by virtually disconnecting the feedback network from M_1. In this case, we consider for the active part $A = g_{m0} / n_{12}$, where g_{m0} is the minimum transconductance of M_1 that guarantees the trigger condition, whereas for the passive part $\beta = V_{gs1} / I_2$. From the analysis of the small-signal circuit in Fig. 3, we obtain:

$$\beta = \frac{V_{gs1}}{I_2} = \frac{I_{wt2}}{sC_{eq}I_2} = \frac{1}{sC_{eq}}\frac{I_{wt2}}{I_{wt1}}\frac{I_{wt1}}{I_2}, \quad (9)$$

$$\frac{I_{wt2}}{I_{wt1}} = \frac{sL_{ms} + R_{cs}}{s(L_{ms} + L_{l2}) + (R_{cs} + R_{wt2}) + 1/sC_{eq}}, \quad (10)$$

$$\frac{I_{wt1}}{I_2} = \frac{r'_{ds}}{sL'_{l1} + r'_{ds} + R'_{wt1} + \dfrac{(sL_{ms} + R_{cs})(sL_{l2} + R_{wt2} + 1/sC_{eq})}{s(L_{ms} + L_{l2}) + (R_{cs} + R_{wt2}) + 1/sC_{eq}}}, \quad (11)$$

where I_{wt2} is the current through R_{wt2} and I_{wt1} is the current through R'_{wt1}. After replacing (10) and (11) in (9), we can rationalize and switch to the frequency domain:

$$\beta = \frac{r'_{ds}\,(i\omega L_{ms} + R_{cs})(a(\omega) - ib(\omega))}{a^2(\omega) + b^2(\omega)}, \quad (12)$$

where a and b are the real and imaginary parts of the denominator of β, which are given by:

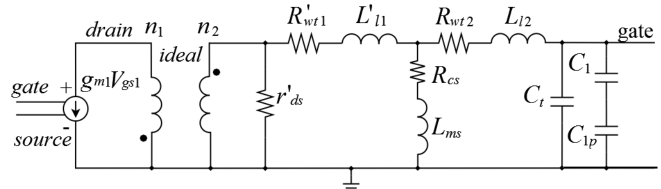

Fig. 3. Simplified small-signal circuit diagram of the step-up oscillator to investigate the mechanism of oscillation at the startup.

$$\begin{aligned} a(\omega) &= -\omega^2 C_{eq}[(r'_{ds} + R'_{wt1})(L_{ms} + L_{l2}) \\ &+ R_{wt2}L_{ms} + R_{cs}L_{l2} + (R_{wt2} + R_{cs})L'_{l1}] + r'_{ds} + R'_{wt1} + R_{cs} \end{aligned}, \quad (13)$$

$$\begin{aligned} b(\omega) &= \omega C_{eq}[(r'_{ds} + R'_{wt1})(R_{wt2} + R_{cs}) + R_{wt2}R_{cs} \\ &- \omega^2 L_{ms}L_{l2} - \omega^2 (L_{ms} + L_{l2})L'_{l1}] + \omega(L_{ms} + L'_{l1}) \end{aligned}, \quad (14)$$

where $\omega = 2\pi f$. In order to determine the frequency of oscillation f_0, we extract the frequency at which the imaginary part of the numerator of (12) is zero [35], which means that:

$$2\pi f_0 L_{ms} a(\omega_0) = R_{cs} b(\omega_0)\,. \quad (15)$$

Hence, by solving (15) we get:

$$f_0 = \frac{1}{2\pi}\sqrt{\frac{1}{C_{eq}}} \cdot \sqrt{\frac{L_{ms}(r'_{ds} + R'_{wt1}) - R_{cs}(L'_{l1} + C_{eq}R_T^2)}{L_{ms}^2(r'_{ds} + R'_{wt1} + R_{wt2}) + L_{l2}L_{ms}(r'_{ds} + R'_{wt1}) + L'_{l1}L_{ms}R_{wt2} - L'_{l1}L_{l2}R_{cs}}} \quad (16)$$

where R_T^2 (Ω^2) is given by:

$$R_T^2 = R_{cs}r'_{ds} + R_{wt2}r'_{ds} + R_{cs}R'_{wt1} + R_{wt2}R'_{wt1} + R_{wt2}R_{cs}\,. \quad (17)$$

Expression (16) includes the leakage inductances L'_{l1}, L_{l2} and the core losses R_{cs}, and gives the approximate onset oscillation frequency. However, the transformer parameters in (16) are generally frequency-dependent. Therefore, in order to predict the effective oscillation frequency we should include in (16) the approximate AC analytical models of L_{ms}, R_{w1}, R_{w2}, and R_{cs}, as shown in [32] and [37], which comprise eddy-current effects and the complex permeability model, together with an estimate (or measure) of the coupling k and of C_{22}. In section IV, equation (16) will be resolved numerically by finding the point at which the oscillation frequency equals the operating frequency of the microtransformer. Now, if we consider a lossy transformer with perfect coupling ($L'_{l1} \approx 0$, $L_{l2} \approx 0$), (16) can be simplified to:

$$f_0 \approx \frac{1}{2\pi}\sqrt{\frac{1}{C_{eq}} \cdot \frac{L_{ms}(r'_{ds} + R'_{wt1}) - R_{cs}C_{eq}R_T^2}{L_{ms}^2(r'_{ds} + R'_{wt1} + R_{wt2})}}\,. \quad (18)$$

Alternatively, if we consider a loosely coupled transformer without core losses ($R_{cs} \approx 0$), (16) can be simplified to:

$$f_0 \approx \frac{1}{2\pi}\sqrt{\frac{1}{C_{eq}} \cdot \frac{r'_{ds} + R'_{wt1}}{L_{ms}(r'_{ds} + R'_{wt1} + R_{wt2}) + L_{l2}(r'_{ds} + R'_{wt1}) + L'_{l1}R_{wt2}}}$$

.(19)

If we neglect both leakage inductances ($L'_{l1} \approx 0$, $L_{l2} \approx 0$) and core losses ($R_{cs} \approx 0$), i.e. loss-less and perfectly coupled transformer, (16) can be shortened to:

$$f_0 \approx \frac{1}{2\pi}\sqrt{\frac{1}{C_{eq}} \cdot \frac{r'_{ds} + R'_{wt1}}{L_{ms}(r'_{ds} + R'_{wt1} + R_{wt2})}}\,, \quad (20)$$

which leads to the general resonant frequency of LC-circuits [35], i.e. $f_0 \cong 1 / [2\pi\,(C_{eq} \cdot L_{ms})^{1/2}]$ by considering $R'_{wt1} >> R_{wt2}$.

Now, if we consider only the real part of (12) and we combine the findings of (15) at resonance, we have that:

$$\beta(f_0) = r'_{ds}\,\frac{R_{cs}\,a(f_0) + 2\pi\,f_0 L_{ms} b(f_0)}{a^2(f_0) + b^2(f_0)} = \frac{r'_{ds}\,R_{cs}}{a(f_0)} \qquad (21)$$

In order to obtain the unity loop gain at resonance as $A(f_0)\,\beta(f_0) = (g_{m0} / n_{12})\,\beta(f_0) = 1$, the minimum g_{m0} of M_1 is:

$$g_{m0} = \frac{n_{12}}{\beta(f_0)} = \frac{n_{12} a(f_0)}{r'_{ds}\,R_{cs}}\,, \qquad (22)$$

which results, after some algebraic steps, in:

$$g_{m0} \approx \frac{n_{12}}{r'_{ds}} \cdot \frac{L_{ms}^2 (r'_{ds} + R'_{wt1}) + L_{l2}^2 R_{cs}}{L_{ms}(L_{ms} + L_{l2})(r'_{ds} + R'_{wt1}) - L_{l2}^2 R_{cs}} + \frac{C_{eq} R_T^2 [(L_{ms} + L_{l2})(r'_{ds} + R'_{wt1}) + 2 L_{l2} R_{cs})]}{L_{ms}(L_{ms} + L_{l2})(r'_{ds} + R'_{wt1}) - L_{l2}^2 R_{cs}}. \qquad (23)$$

Equation (23) is obtained by considering a step-up transformer with $n_{12} >> 1$, $L'_{l1} \approx L_{l2}$ from (5), $R'_{wt1} >> R_{wt2}$, and hence $R_T^2 \approx R_{cs}\,(r'_{ds} + R'_{wt1})$. Now, if we consider a loosely coupled transformer without core losses ($R_{cs} \approx 0$), (23) can be simplified to:

$$g_{m0} \approx \frac{n_{12}}{r'_{ds}} \cdot \frac{L_{ms}}{L_{ms} + L_{l2}}\,. \qquad (24)$$

Besides, if we consider a lossy transformer with perfect coupling ($L'_{l1} \approx L_{l2} \approx 0$), (23) can be simplified as:

$$g_{m0} \approx \frac{n_{12}}{r'_{ds} L_{ms}} \cdot (C_{eq} R_T^2 + L_{ms})\,. \qquad (25)$$

Finally, if we neglect both leakage inductances ($L'_{l1} \approx L_{l2} \approx 0$) and core losses ($R_{cs} \approx 0$), i.e. loss-less and perfectly coupled transformer, (23) can be reduced to:

$$g_{m0} \approx \frac{n_{12}}{r'_{ds}} = \frac{1}{r_{ds} n_{12}}\,. \qquad (26)$$

Now, if we neglect V_{ds1} in (8) because of the small values of V_{teg} considered, we obtain that $g_{ds1} \approx -\beta_{n1}\,V_{tn1}$ and thus $r_{ds} \approx 1 / (-\beta_{n1}\,V_{tn1})$. In this case, (26) becomes:

$$g_{m0} \approx -\frac{\beta_{n1} V_{tn1}}{n_{12}}\,. \qquad (27)$$

Additionally, we can extract the minimum source voltage V_{teg0} by inverting (7) and using g_{m0} instead of g_{m1} as follows:

$$V_{teg0} \approx \frac{g_{m0}}{\beta_{n1}} \cdot (1 - R_{eq} \beta_{n1} V_{tn1})\,. \qquad (28)$$

Now, by substituting (27) in (28) we obtain:

$$V_{teg0} \approx -\frac{V_{tn1}}{n_{12}} \cdot (1 - R_{eq} \beta_{n1} V_{tn1})\,. \qquad (29)$$

In order to minimize the first factor in (29), the step-up transformer should have a large n_{12}, while the n-type MOSFET should have a small $|V_{tn1}|$. In order to minimize the second factor $(1 - R_{eq}\,\beta_{n1}\,V_{tn1})$, we should reduce again $|V_{tn1}|$ together with R_{eq} and β_{n1}. In Section IV this design optimization will be discussed in depth. Finally, the Barkhausen criterion is fulfilled if g_{m1} is greater than the g_{m0} given in (22)-(27), or if V_{teg} is greater than the V_{teg0} given in (28)-(29), as:

$$g_{m1} \geq g_{m0} \quad \text{or} \quad V_{teg} \geq V_{teg0}\,. \qquad (30)$$

Equation (30) sets the startup condition in order for oscillations to occur. Since few and mainly qualitative analyses are present in literature [18] [26] for this kind of circuits, relationships (16), (18)-(20), (22)-(27), and (28)-(29) represent new analytical expressions for calculating respectively f_0, g_{m0}, and V_{teg0}, in a Meissner-type oscillator topology with a potential lossy and loosely coupled step-up microtransformer.

C. *Properties of the Bond Wire Microtransformers*

Two 1:n_2 bond wire transformers on a PCB substrate were used (Fig. 4). The first is the 1:38 turns toroidal MnZn 75 ferrite core reported in [32], with a ≅24 mm² area and inductance per unit area of 12.8 μH/mm² up to 0.3 MHz. The second is a 1:52 toroidal race-track shaped 40011 ferromagnetic LTCC core similar to that shown in [34], with a ≅28 mm² area and 1.1 μH/mm² up to several MHz. Since the oscillation frequency f_0 described in (16), (18)-(20) depends mainly on L_{ms} and C_{eq}, in order to limit high-frequency effects the transformer should have a large L_{22} along with a good coupling k to reduce f_0 with a fixed C_{eq}. Besides, a high turns ratio n_{12}, i.e. high L_{22} / L_{11}, is further required as shown in (28)-(29) to allow lower startup voltages. On the other hand, integrated capacitors have limited values which impose restrictions on C_{eq}, and thus on the minimum achievable f_0.

The ferrite core outer D_o and inner D_i diameters are 3.95 mm and 2.15 mm, whereas the thickness is 0.45 mm. Since two pairs of bonding wires were found to be short-circuited, the actual turns ratio of the MnZn 75 device is 1:36. The LTCC core size is 7.0×3.0×0.4 mm³ ($l \times w \times h$), with a 1 mm core width. The LTCC core device is assembled with 25 μm gold bonding wires on a PCB substrate with copper metallizations with 90 μm width, 60 μm minimum spacing, and 16 μm thickness. The one-turn mean metal and wire length are respectively 1.7 and 2.1 mm, the bond pad pitch is 150 μm, and the outer-inner pad distances from the core are respectively 450 and 225 μm. The LTCC core has relative permeability $\mu_{rc} \approx 200$, resistivity $\rho_c > 10^8$ Ω·cm, saturation flux density $B_s \approx 300$ mT, mean magnetic path length $l_c \approx 14.3$ mm, and cross-section $A_c \approx 0.40$ mm². The -3dB frequency and bandwidth of the inductive μ'_{rs} and resistive μ''_{rs} relative permeabilities, respectively, are estimated to be $f_H \approx 9.6$ MHz and $\Delta f \approx 1.0$ MHz, as discussed in [32] [37].

The MnZn 75 core [32] has a higher permeability compared to the ferromagnetic LTCC core thus ensuring higher self-inductances but nevertheless high series resistances due to greater eddy currents in both windings and core. Besides this, the LTCC core [38]-[40] has a lower permeability and a higher resistivity which allow to reduce the high-frequency effects while providing lower self-inductances.

IV. Experimental Results and Model Validation

This section illustrates the modeling results and the startup measurements obtained with both bond wire transformers.

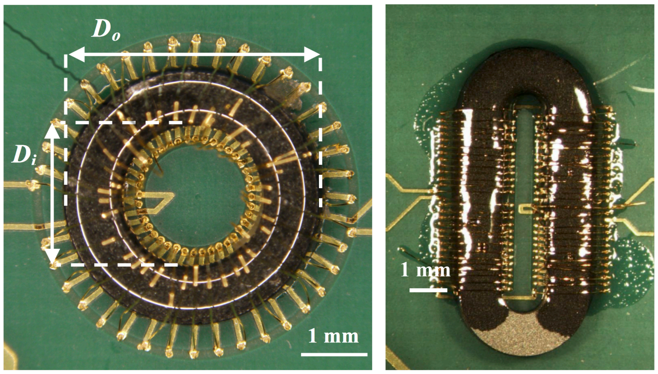

Fig. 4. The bond wire microtransformers used for validation: 1:38 turns with MnZn 75 core (left), and 1:52 turns with 40011 ferromagnetic LTCC core (right).

The energy source voltage V_{teg} is assumed to be in the 50-250 mV range by assuming the 10 mV/K Seebeck coefficient of the CP14 module [36] and a 5-25 K temperature gradient between cold and hot side. These are typical values for wearable or industrial applications. Fig. 5 shows a microphotograph of the IC with the top metal pads compatible with bond wire micromagnetics. The die area is 15 mm^2, and the area of the sole step-up oscillator in Fig. 1, composed by the active (i.e. M_1, M_2, M_3) and passive (i.e. capacitors) parts, is about 0.6 mm^2. The remaining area contains a series of unused integrated capacitors and MOSFETs that can be optionally connected. Besides, the measured parasitic resistances of connections are $R_{con1} \approx 2.35\ \Omega$ and $R_{con2} \approx 1.93\ \Omega$ for the primary and secondary side. For M$_1$, we have $\beta_{n1} = 0.3157$ A/V^2, and $C_{gs1} \cong 3.0$ pF. The values used in the experiment (see Fig. 1) are: $R_{teg} = 0.43\ \Omega$ [36], $C_{in} = 390$ nF, $C_{out} = 100$ nF, and $R_{out} = 10$ MΩ. The latter is chosen to represent the typical current drawn by a supervisor circuit whose duty is the activation of the conventional power converter once the step-up oscillator has made the minimum supply voltage available.

A. Startup with Ferrite Core Microtransformer

The MnZn 75 core has a higher permeability ($\mu_{rc} \approx 5000$) and a lower resistivity ($\rho_c = 3\cdot10^2\ \Omega\cdot$cm) than the LTCC core. This enhances L_{11}, L_{22} at the expense of higher R_{11}, R_{22} due to higher core losses. However, this device has a very good k. By combining into (16) the approximate AC analytical model (extrapolated from core material and impedance measurements in [32]) of the 1:36 turns MnZn 75 device, we can determine numerically the effective oscillation frequency.

Let us now recall that $r'_{ds} = n_{12}^2 / g_{ds1}$, with $g_{ds1} \cong -\beta_{n1} V_{tn1}$ since $|V_{tn1}| >> V_{ds1}$, as previously discussed. Fig. 6 shows the expression of f_0 in (16) as a function of frequency obtained with $C_{22} < 1$ pF (estimated from [37]), $C_{par} \approx 25$ pF, and thus $C_t \approx C_{22}+C_{gs1}+ C_{par} \approx 29$ pF, $C_1 = 150$ pF, $C_{1p} = 10$ pF, and thus $C_{eq} = C_t + (C_1 C_{1p}) / (C_1+C_{1p}) = 39$ pF.

TABLE I
MICROTRANSFORMER PARAMETERS.

Core	L_m (nH)	L_{ms} (µH)	L_{l1} (nH)	L_{l2} (µH)	R_{w1} (Ω)	R_{w2} (Ω)	R_{cs} (Ω)	k
MnZn	130	165	14.4	18.3	0.2	5.5	1260	0.9
LTCC	6.8	18.4	5.3	14.5	0.15	8.1	10.7	0.56

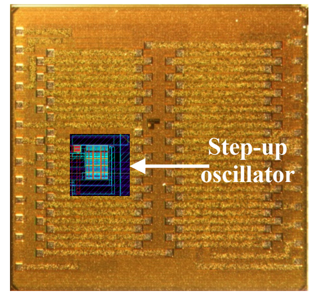

Fig. 5. Microphotograph of the IC designed in a STMicroelectronics 0.32 µm BCD technology. The step-up converter layout is shown inside.

The effective oscillation frequency (denoted as f'_0) is the point where the frequencies in the xy-axes match ($f'_0 \approx 1.45$ MHz). Hence, the transformer parameters at f'_0 from [32] are summarized in Table I.

In order for oscillations to occur, we must design M_1 or set external conditions so that $g_{m1} \geq g_{m0}$ or $V_{teg} \geq V_{teg0}$ as stated in (30). Fig. 7 shows the transconductances g_{m1} in (7) and g_{m0} in (22) versus V_{teg}, and demonstrates that the converter starts to oscillate when $g_{m1} \geq g_{m0}$ which happens at $V_{teg0} \approx 200$ mV with $g_{m1} = g_{m0} \approx 28$ mS. Fig. 8 shows on the top the same g_{m0} and g_{m1} (with $V_{teg} = 200$ mV, 220 mV) versus β_{n1}, and explains that the startup condition $g_{m1} \geq g_{m0}$ happens for 0.1 A/V$^2 \leq \beta_{n1} \leq 4.5$ A/V^2 with $V_{teg} = 220$ mV, whereas the useful range of β_{n1} shrinks with $V_{teg} = 200$ mV. Hence, the chosen value $\beta_{n1} = 0.3157$ A/V^2 represents a good compromise for oscillations to occur. Furthermore, Fig. 8 illustrates on the bottom the strong dependence of f'_0 on the gain β_{n1}. Hence, as a general rule we can deduce that reducing β_{n1} implies dropping the startup and MOSFET transconductances, i.e. reducing the minimum source voltage, at the cost of higher oscillation frequencies and thus of higher core losses. The main parameters of the small-signal analysis are shown in Table II.

Fig. 9 shows on the top g_{m0} and g_{m1} versus V_{tn1} with the chosen β_{n1} and $V_{teg} = 200$ mV, whereas on the bottom the dependence of f'_0 on V_{tn1} is depicted. We can assess that decreasing $|V_{tn1}|$ allows to increase g_{m1} and to decrease g_{m0}, however at the cost of higher oscillation frequencies. Fig. 10 shows further the contour plot of g_{m0} with $V_{teg} = 200$ mV as a function of V_{tn1} and β_{n1}.

In order to set-up the startup conditions, Fig. 11 plots the starting isosurface as a function of (V_{tn1}, β_{n1}, V_{teg}) obtained by evaluating if $g_{m1} \geq g_{m0}$ is verified: if this is true, the point is located on or above the isosurface. The combinations below the isosurface do not permit oscillations. We see that the minimum allowable $V_{teg} = V_{teg0}$ for which oscillations occur is ≈25 mV, and can be potentially obtained if (V_{tn1}, β_{n1}) = (-0.1 V, 6 A/V^2). We remark that the plots from Fig. 8 to Fig. 11 assume that the transformer parameters remain constant.

An Agilent E3631 power supply is used for emulating the voltage source. Experimental tests are performed on the startup converter with the 1:36 turns MnZn 75 device. The circuit starts oscillating and increasing the output voltage from input source voltages down to $V_{teg} \cong 228$ mV. If $V_{teg} \cong 260$ mV, the steady-state rectified output voltage is $V_{rect} \cong 0.7$ V, which is sufficient to start a standard boost

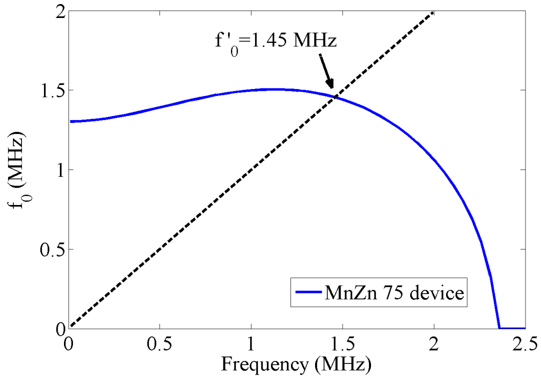

Fig. 6. Oscillation frequency f_0 as a function of frequency with $W_1 = 2$ mm for the step-up oscillator with the 1:36 turns MnZn 75 core transformer. The dashed black line is the bisector of the graph.

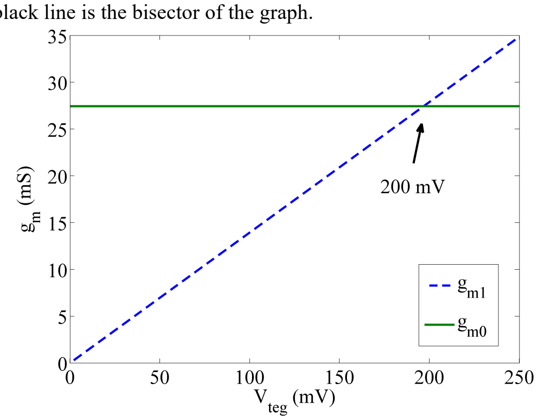

Fig. 7. Transconductances g_{m1} and g_{m0} versus source voltage V_{teg} with the chosen β_{n1} and with the 1:36 turns MnZn 75 core transformer.

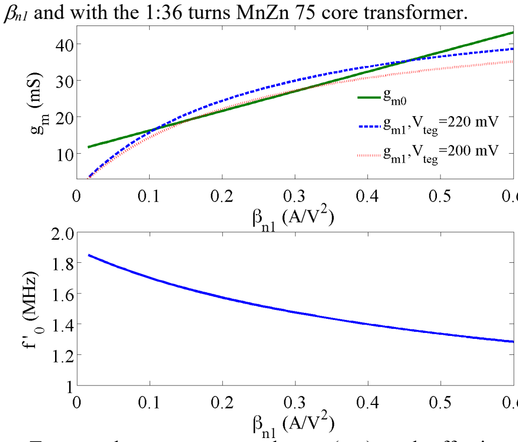

Fig. 8. Transconductances g_{m1} and g_{m0} (top) and effective oscillation frequency f'_0 (bottom) versus gain β_{n1} for the step-up oscillator with the 1:36 turns MnZn 75 core transformer.

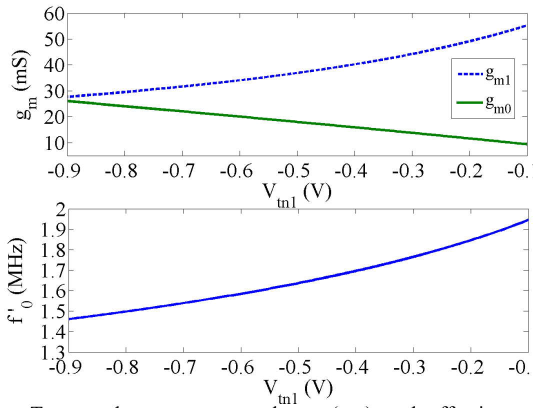

Fig. 9. Transconductances g_{m1} and g_{m0} (top) and effective oscillation frequency f'_0 (bottom) versus M_1 threshold voltage V_{tn1} with the chosen β_{n1}, $V_{teg} = 200$ mV, and the 1:36 turns MnZn 75 core transformer.

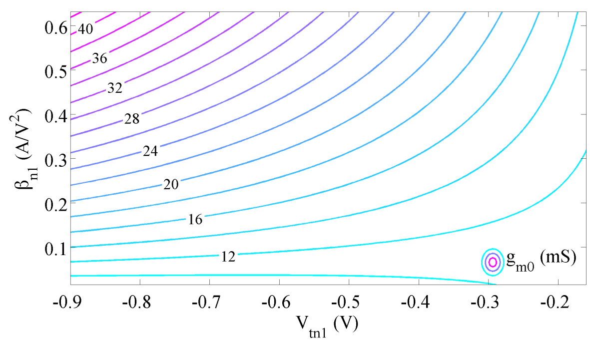

Fig. 10. Contour plot of g_{m0} as a function of M_1 threshold voltage V_{tn1} and gain β_{n1} with $V_{teg} = 200$ mV and the 1:36 turns MnZn 75 core transformer.

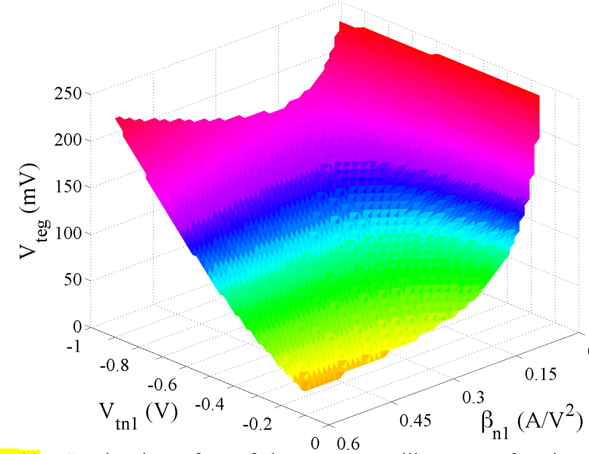

Fig. 11. Starting isosurface of the step-up oscillator as a function of M_1 threshold voltage V_{tn1}, gain β_{n1}, and source voltage V_{teg} with the 1:36 turns MnZn 75 core transformer. The points (V_{tn1}, β_{n1}, V_{teg}) under the isosurface do not allow oscillation, whereas the combinations on or above the isosurface permit oscillations.

converter or a charge pump with reasonable efficiency. This is in good agreement with the analytical results described previously, which report $V_{teg0} \approx 200$ mV. Fig. 12 displays the experimental startup waveforms obtained by increasing V_{teg}, while Fig. 13 depicts the steady-state oscillating waveforms associated to Fig. 12 for time $t \geq 25$ s with a measured oscillation frequency of ≈ 1.36 MHz, which is very close to the expected $f'_0 \approx 1.45$ MHz. The data in Figs. 12 and 13 are acquired through a digital sampling oscilloscope Tektronix MSO 2024.

B. Startup with Magnetic LTCC Core Microtransformer

The 40011 magnetic LTCC core has a lower permeability ($\mu_{rc} \approx 200$) and a higher resistivity ($\rho_c > 10^8$ Ω·cm) than the MnZn 75 core. This reduces L_{11}, L_{22} with the benefit of lower R_{11}, R_{22}, i.e. lower core losses, due to the higher resistivity. However, the transformer is loosely coupled, i.e. it has lower k than the MnZn 75 device. As before, by joining into (16) the approximate AC analytical model of the 1:52 turns 40011 LTCC device based on [34], we can determine numerically f'_0.

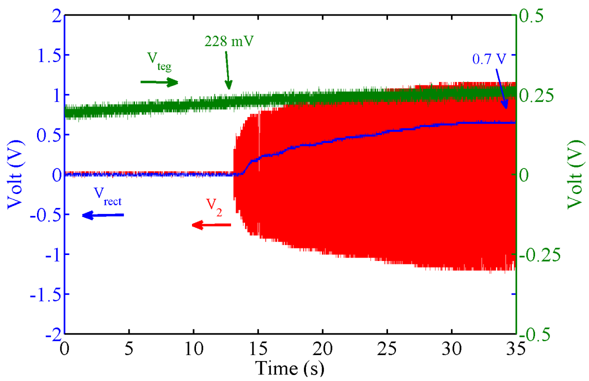

Fig. 12. Experimental startup waveforms: source voltage V_{teg}, secondary voltage V_2, and rectified output voltage V_{rect} for the step-up oscillator with the 1:36 turns MnZn 75 core transformer. V_2 and V_{rect} are referred to the left y-axis and V_{teg} to the right y-axis.

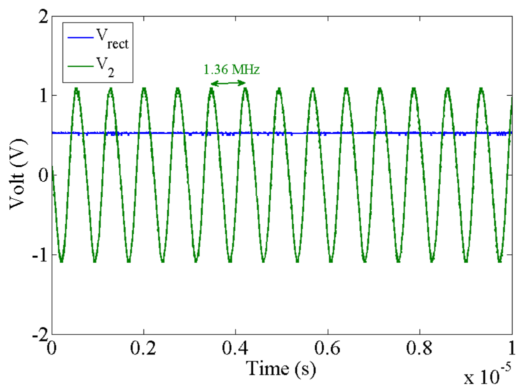

Fig. 13. Experimental oscillating waveforms: secondary voltage V_2, and rectified output voltage V_{rect} for the step-up oscillator with the 1:36 turns MnZn 75 core transformer.

TABLE II
MAIN TRANSFORMER AND DIFFERENTIAL PARAMETERS.

Core	n_{12}	L'_{l1} (μH)	R'_{wt1} (kΩ)	R_{wt2} (Ω)	R_{eq} (Ω)
MnZn	36	18.7	3.86	7.43	4.48
LTCC	52	14.4	7.92	10	2.93
Core	C_{eq} (pF)	g_{m1} (mS)	g_{m0} (mS)	f'_0 (MHz)	V_{teg0} (mV)
MnZn	39	30.6	28	1.45	200
LTCC	84	15.5	12.1	3.03	71

Fig. 14 plots on the top the expression of f_0 in (16) as a function of frequency obtained with $C_{22} < 1$ pF (estimated from [37]), $C_{par} \approx 40$ pF, and thus $C_t \approx C_{22}+C_{gs1}+C_{par} \approx 44$ pF, $C_1 = 600$ pF, $C_{1p} = 40$ pF, and thus $C_{eq} = C_t + (C_1\, C_{1p}) / (C_1+C_{1p}) = 84$ pF. The effective oscillation frequency is located at $f'_0 \approx 3.03$ MHz. The values of the transformer parameters at f'_0 are summarized in Table I. Fig. 14 on the bottom shows the transconductances g_{m1} in (7) and g_{m0} in (22) versus V_{teg} with the chosen β_{n1}, and proves that the converter starts to oscillate at $V_{teg0} \approx 71$ mV with $g_{m1} = g_{m0} \approx 12.1$ mS. Fig. 15 displays on the top the same g_{m0} and g_{m1} (with $V_{teg} = 71$ mV, 90 mV) as a function of β_{n1}, and clarifies that the startup condition $g_{m1} \geq g_{m0}$ occurs for 0.1 A/V$^2 \leq \beta_{n1} \leq 0.7$ A/V^2 with $V_{teg} = 90$ mV. Besides, f'_0 does not change significantly with β_{n1}. Reducing β_{n1} involves reducing the startup and MOSFET transconductances, i.e. reducing the minimum source voltage, without substantial drawbacks. The main parameters of the small-signal analysis with $V_{teg} = 90$ mV are reported in Table II.

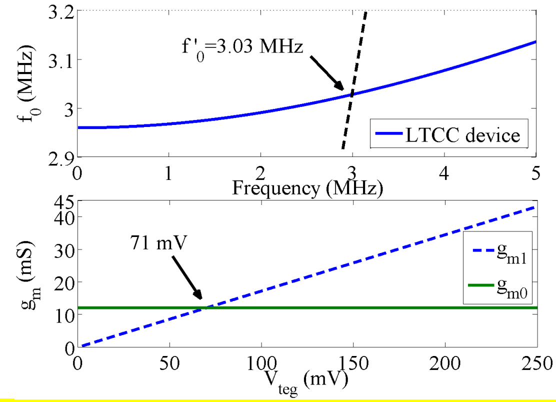

Fig. 14. Oscillation frequency f_0 as a function of frequency (top) and transconductances g_{m1} and g_{m0} (bottom) versus source voltage V_{teg} with $W_1 = 2$ mm for the step-up oscillator with the 1:52 turns 40011 LTCC core transformer.

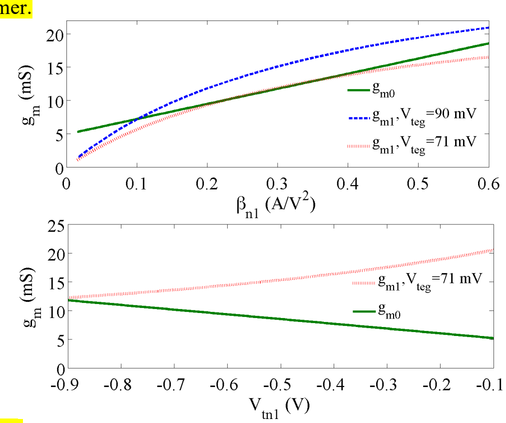

Fig. 15. Transconductances g_{m1} and g_{m0} versus M_1 gain β_{n1} (top), and threshold voltage V_{tn1} with the chosen β_{n1} (bottom), with the 1:52 turns LTCC core transformer.

Let us now set $r'_{ds} = n_{12}^2 / g_{ds1}$, where g_{ds1} is derived from (8). Fig. 15 illustrates on the bottom g_{m0} and g_{m1} versus V_{tn1} with the chosen β_{n1} and $V_{teg} = 71$ mV. Decreasing $|V_{tn1}|$ increases g_{m1} and decreases g_{m0}, without significant changes of f'_0.

Fig. 16 plots the starting isosurface as a function of (V_{tn1}, β_{n1}, V_{teg}). The minimum $V_{teg} = V_{teg0}$ for which oscillations might happen is ≈ 10 mV, obtained in case (V_{tn1}, β_{n1}) = (-0.1 V, 0.6 AV^{-2}). The plots in Figs. 15 and 16 assume constant transformer parameters, which is reasonably true because f'_0 is quite insensitive from β_{n1} and V_{tn1}.

Experimental tests are performed on the startup converter with the 1:52 turns 40011 LTCC device achieving oscillations with input voltages down to $V_{teg} \cong 104$ mV. When $V_{teg} \cong 152$ mV, a steady-state rectified output $V_{rect} \cong 0.7$ V is provided. This is in satisfactory agreement with the analytical results illustrated before, which report $V_{teg0} \approx 71$ mV. Fig. 17 shows the experimental startup waveforms obtained by increasing V_{teg} up to 104 mV and above. At steady-state we obtain a measured oscillation frequency of ≈ 2.88 MHz, which is reasonably close to the effective $f'_0 \approx 3.03$ MHz. The same equipment is used for the stimulus and for acquiring the data.

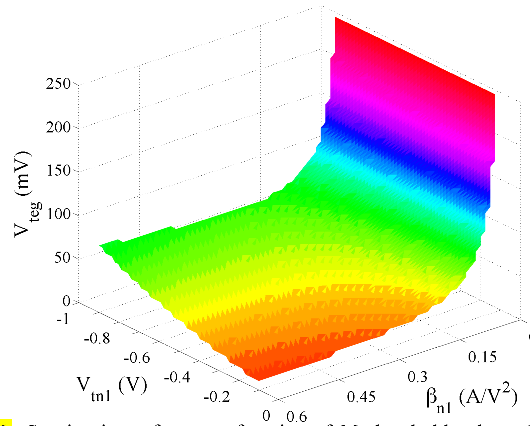

Fig. 16. Starting isosurface as a function of M_1 threshold voltage V_{tn1}, gain β_{n1}, and source voltage V_{teg} with the 1:52 turns 40011 LTCC core transformer. Oscillations occur for points (V_{tn1}, β_{n1}, V_{teg}) above the surface.

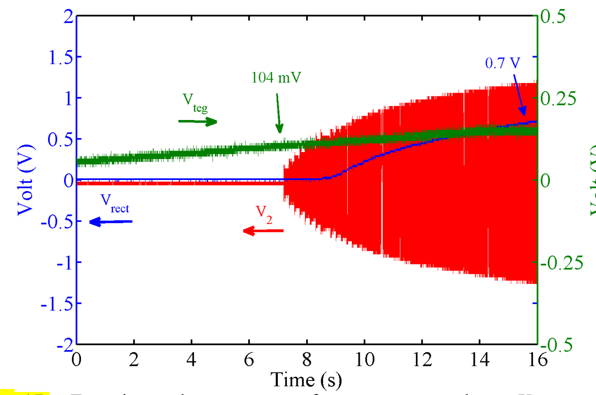

Fig. 17. Experimental startup waveforms: source voltage V_{teg}, secondary voltage V_2, and rectified output voltage V_{rect} for the step-up oscillator with the 1:52 turns 40011 LTCC core transformer.

V. Conclusions

This work achieves a measured minimum startup voltage of ≈100 mV obtained by coupling the low-voltage oscillator IC and an LTCC core bond wire transformer. As a new element, with respect to Meissner-type oscillators presented in literature, this work has investigated the effects of core losses and leakage inductances on the startup requirements, and has provided a complete analytical model of the whole circuit with lossy microtransformers. The analysis highlights the trade-offs between MOSFET design and technological parameters, i.e. β_{n1} and V_{tn1}, and the microtransformer parameters, i.e. L_{ms}, k, and n_{12}, in order to reduce the minimum transconductance g_{m0} and the minimum startup voltage V_{teg0}.

As an additional key point, the step-up oscillator IC validates the proposed model. We also remark that literature reports lower activation voltages based on mechanical switches [13], and on off-chip or SMD transformers [18] [19] [24]-[26]. The circuits in [18] and [27] start respectively from 40 mV and 20 mV, and rely on larger better-coupled off-chip transformers with higher inductances and turns-ratios of 1:60 and 1:100. In addition, the amplifier FET in [18] has a very favorable threshold voltage of -15 mV. However, the proposed approach based on bond wire magnetics allows direct die-level integration of the magnetic part, as in [34]. Lower startup voltages can be achieved, e.g. down to ≈10 mV, by tuning design parameters, or by using more efficient microtransformers.

References

[1] M. Raju, "Energy harvesting, ULP meets energy harvesting: a game-changing combination for design engineers," White paper. Texas Instruments Inc., 2008.

[2] D. M. Rowe, *CRC Handbook of Thermoelectric*, CRC Press, 1995.

[3] H. Bottner, J. Nurnus, A. Schubert, F. Volkert, "New high density micro structured thermogenerators for stand alone sensor systems," *Proc. of Thermoelectrics Conf.*, 2007, pp. 306-309.

[4] P.-H. Chen, K. Ishida, K. Ikeuchi, X. Zhang, K. Honda, Y. Okuma, Y. Ryu, M. Takamiya, T. Sakurai, "Startup techniques for 95 mV step-up converter by capacitor pass-on scheme and V_{TH}-tuned oscillator with fixed charge programming," *IEEE J. Solid-State Circuits*, vol. 47, no. 5, pp.1252-1260, May 2012.

[5] J. M. Damaschke, "Design of a low-input-voltage converter for thermoelectric generator," *IEEE Trans. Ind. Appl.,* vol.33, no.5, pp.1203-1207, 1997.

[6] P. Fiorini, I. Doms, C. Van Hoof, R. Vullers, "Micropower energy scavenging, " *Proc. 34th Solid-State Circuits Conf.*, Edinburgh, UK, pp. 4-9, 2008.

[7] J. W. Kimball, T. L. Flowers, P. L. Chapman, "Low-input-voltage, low-power boost converter design issues, " *IEEE Power Electron. Lett.*, vol. 2, no. 3, pp. 96-99, 2004.

[8] N. Degrenne, B. Allard, F. Buret, F. Morel, S.-E. Adami, D. Labrousse, "Comparison of 3 self-starting step-up DC:DC converter topologies for harvesting energy from low-voltage and low-power microbial fuel cells," *Proc. 14th Power Electron. and Appl. Conf.*, Birmingham, UK, pp.1-10, 2011.

[9] S.-E. Adami, V. Marian, N. Degrenne, C. Vollaire, B. Allard, F. Costa, "Self-powered ultra-low power DC-DC converter for RF energy harvesting," *Faible Tension Faible Consommation (FTFC), 2012 IEEE* , Paris, FR, pp.1,4, June 2012.

[10] P.-H. Chen, K. Ishida, X. Zhang, Y. Okuma, Y. Ryu, M. Takamiya, T. Sakurai, "0.18-V input charge pump with forward body biasing in startup circuit using 65nm CMOS," *Proc. IEEE Custom Integr. Circuits Conf.*, San Jose, CA, pp.1-4, 2010.

[11] B. Mishra, C. Botteron, P. A. Farine, "A 120 mV startup circuit based on charge pump for energy harvesting circuits," *IEICE Electron. Express*, vol. 8, no. 11, pp. 830-834, 2011.

[12] P.-H. Chen, K. Ishida, X. Zhang, Y. Okuma, Y. Ryu, M. Takamiya, T. Sakurai, "A 120-mV input, fully integrated dual-mode charge pump in 65-nm CMOS for thermoelectric energy harvester," *Proc. IEEE 17th Asia and South Pacific - Design Autom. Conf.*, Sydney, NSW, pp.469-470, 2012.

[13] Y. K. Ramadass, A. P. Chandrakasan, "A battery-less thermoelectric energy harvesting interface circuit with 35 mV startup voltage," *IEEE J. Solid-State Circuits*, vo. 46, no. 1, pp. 333-341, 2011.

[14] E. J. Carlson, K. Strunz, B. P. Otis, "A 20 mV input boost converter with efficient digital control for thermoelectric energy harvesting, "*IEEE J. Solid-State Circuits*, vol. 45, no. 4, pp. 741-750, 2010.

[15] L. Mateu, M. Pollak, P. Spies, "Step-up converters for human body energy harvesting thermogenerators," *Proc. 7th Int. Workshop on Micro and Nanotechnol. for power generation and energy conversion appl.*, pp. 213-216, 2007.

[16] M. Pollak, L. Mateu, P. Spies, "Step-up DC-DC converter with coupled inductors for low input voltages," *Fraunhofer IIS*, 2008.

[17] N. Degrenne, F. Buret, F. Morel, S.-E. Adami, D. Labrousse, B. Allard, A. Zaoui, "Self-starting DC:DC boost converter for low-power and low-voltage microbial electric generators," *IEEE Energy Convers. Congr. and Expo.*, pp. 889-896, Phoenix, AZ, 2011.

[18] J.-P. Im, S.-W. Wang, S.-T. Ryu, G.-H. Cho, "A 40 mV Transformer-reuse self-startup boost converter with MPPT control for thermoelectric energy harvesting," *IEEE J. Solid-State Circuits*, vol. 47, no. 12, pp. 3055-3067, 2012.

[19] P.-S. Weng, H.-Y. Tang, P.-C. Ku, L.-H. Lu, "50 mV-input batteryless boost converter for thermal energy harvesting," *IEEE J. Solid-State Circuits*, vol. 48, no. 4, pp. 1031-1041, 2013.

[20] K. Kadirvel, Y. Ramadass, U. Lyles, J. Carpenter, V. Ivanov, V. McNeil, A. Chandrakasan, B. Lum-Shue-Chan, "A 330nA energy-harvesting charger with battery management for solar and thermoelectric

energy harvesting," *Proc. IEEE Int. Solid-State Circuits Conf. Digest of Technical Papers*, San Francisco, CA, pp. 106-108, 2012.

[21] I. Doms, P. Merken, R. Mertens, C. Van Hoof, "Integrated capacitive power-management circuit for thermal harvesters with output power 10 to 1000uW," *Proc. IEEE Int. Solid-State Circuits Conf. Digest of Technical Papers*, San Francisco, CA, pp. 300-302, 2009.

[22] J. Kim, C. Kim, "A DC-DC boost converter with variation-tolerant MPPT technique and efficient ZCS circuit for thermoelectric energy harvesting applications," *IEEE Trans. Power Electron*, vol. 28, no. 8, pp. 3827-3833, 2013.

[23] A. A. Blanco, G. A. Rincon-Mora, "A 44–93-μs 250–400-mV 0.18-μm CMOS starter for dc-sourced switched-inductor energy harvesters," *IEEE Trans. Circuits and Syst. II: Express Briefs*, vol. 61, no. 12, pp.1002-1006, Dec. 2014.

[24] Y.-K. Teh, P. K. T. Mok, "Design of transformer-based boost converter for high internal resistance energy harvesting sources with 21 mV self-startup voltage and 74% power efficiency," *IEEE J. Solid-State Circuits*, vol. 49, no. 11, pp. 2694-2704, Nov. 2014.

[25] Z. Haozhou, Z. Menglian, S. Liu, Y. Fang, X. Wu, "A 20-300mV transformer-based self-startup flyback converter with MPPT and ZCS control for thermoelectric energy harvesting," *Proc. IEEE Circuits and Syst. (MWSCAS), 57th International Midwest Symposium*, College-Station, TX, pp. 41-44, Aug. 2014.

[26] V. D. Nachiket, Y. Ramadass, A. P. Chandrakasan, "A bipolar ±40 mV self-starting boost converter with transformer reuse for thermoelectric energy harvesting," *Proc. ISLPED 2014*, New York, USA, pp. 221-226, 2014.

[27] Linear Technology. *LTC3108 – Ultralow voltage step-up converter and power manager, 20120,*
url: http://cds.linear.com/docs/en/datasheet/3108fc.pdf

[28] EnOcean. *ECT-310 – Ultra-low power DC-DC converter for thermal energy*, 2012,
url: http://www.enocean.com/en/enocean_modules_902mhz/ect-310-perpetuum/

[29] Coilcraft. *LPR6235 – Miniature step-up flyback transformers,* 2010. url: http://www.coilcraft.com/pdfs/lpr6235.pdf

[30] Coilcraft. *LPR4012 – Miniature step-up flyback transformers,* 2010. url: http://www.coilcraft.com/pdfs/lpr4012.pdf

[31] C. O. Mathúna, N. Wang, S. Kulkarni, S. Roy, "Review of integrated magnetics for power supply on chip (PwrSoC)," *IEEE Trans. Power Electron.*, vol.27, no.11, pp.4799-4816, Nov. 2012.

[32] E. Macrelli, A. Romani, N. Wang, S. Roy, M. Hayes, R. P. Paganelli, C. Ó Mathúna, M. Tartagni, "Modeling, design, and fabrication of high-inductance bond wire microtransformers with toroidal ferrite core," *IEEE Trans. Power Electron.,* vol.PP, no.99, pp.1-1, doi: 10.1109/TPEL.2014.2370814 (in press),

[33] E. Macrelli, N. Wang, S. Roy, M. Hayes, R. P. Paganelli, M. Tartagni, A. Romani, "Design and fabrication of a 315 μH bondwire micro-transformer for ultra-low voltage energy harvesting," *Proc. Design, Autom. and Test in Europe Conf. (DATE)*, Dresden, pp.1-4, Mar 2014.

[34] E. Macrelli, A. Romani, N. Wang, S. Roy, M. Hayes, R. P. Paganelli, M. Tartagni, "Design and fabrication of a 29 μH bondwire micro-transformer with LTCC magnetic core on silicon for energy harvesting applications," *Procedia Engineering,* vol.87, pp.1557-1560, 2014.

[35] G. Gonzalez, *Foundations of oscillator circuit design*, A. House, 2007.

[36] Laird Technologies. *CP Series CP14,31,045 thermoelectric modules,* 2013. url: http://www.lairdtech.com/products/cp14-31-045-l1-w45

[37] M. K. Kazimierczuk, *High-Frequency Magnetic Components*, John Wiley & Sons, 2014, Second edition.

[38] P. L. Fulmek, P. Haumer, I. Atassi, B. Schweighofer, H. Wegleiter, "Magnetic DC-properties of LTCC-ferrite material and their temperature dependence," *IEEE Trans. Magn.*,vol.48, no.4, pp.1541-1544, 2012.

[39] A. H. Feingold, M. Heinz, R. L. Wahlers, M. A. Stein, "Materials for capacitive and inductive components integrated with commercially available LTCC systems," *Proc. IMAPS 2003*, 2003.

[40] M. Mu, W. Zhang, F. C. Lee, Y. Su, "Laminated low temperature co-fired ceramic ferrite materials and the applications for high current POL converters," *Proc. Energy Convers. Congr. and Expo.*, Denver, CO, pp. 621-627, 2013.

Enrico Macrelli received the B.S. and M.S. degrees in electronic and telecommunications engineering in 2007 and 2009, respectively, and the Ph.D. degree in information technology in 2014, all from the University of Bologna, Bologna, Italy. In 2012 he joined the Tyndall National Institute, Cork, Ireland, as visiting student, and worked on design and fabrication of magnetic materials and components. Since 2015 he has been Postdoctoral Researcher at the Department of Electrical and Computer Engineering of the National University of Singapore, Singapore. His research interests include design techniques for carbon dioxide sensors and micro-power energy harvesting systems.

Aldo Romani received the Dr. Eng. degree in electrical engineering and Ph.D. degree in electrical engineering, computer science, and telecommunications from the University of Bologna, Bologna, Italy, in 2001 and 2005, respectively. In 2008, he joined the University of Bologna, Cesena, Italy, as an Assistant Professor. He has authored or coauthored over 40 international scientific publications. He has been involved with CMOS integrated sensors, applications of piezoelectric materials, and energy harvesting systems. Dr. Romani was a co-recipient of the 2004 Jan Van Vessem Award of the IEEE International Solid-State Circuits Conference.

Rudi P. Paganelli received the Dr. Eng. degree in electrical engineering in 1998 and the Ph.D. degree in electrical engineering, computer science and telecommunications in 2002 from the University of Bologna, Bologna, Italy. In 2002 he joined the CNR-IEIIT in Bologna as a Research Fellow, and since 2003, he has been an Assistant Professor for the course of power electronics at the University of Bologna. His research interests include electronic device modeling, design techniques for microwave circuits, nonlinear circuits and power electronics.

Antonio Camarda received the B.S. and M.S. degrees in electronic engineering from the Polytechnic University of Bari, Italy, in 2006 and 2010, respectively. For a year and a half he has been a SAP IT Consultant. In 2011 he joined the University of Bologna–STMicroelectronics lab as analog IC designer. Since 2012 he has been working towards the Ph.D. degree in information technology at the University of Bologna, Italy. His research interests include integration of magnetic devices and design techniques for low-power ICs.

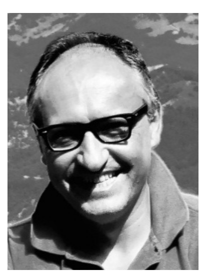

Marco Tartagni (M'99) received the M.S. in electrical engineering in 1988 and the Ph.D. in electrical engineering and computer sciences in 1993 both from the University of Bologna, Bologna, Italy. In 1994 he joined the Department of Electrical Engineering at the California Institute of Technology, Pasadena, CA as a Research Fellow. Since March 1995 he has been with the Department of Electronics, University of Bologna, where he is currently an Associate Professor. In 1997, he designed the first silicon-only fingerprint capacitive sensor. In 1999, he co-founded the company Silicon Biosystems active in the field of lab-on-a-chip devices. From 2005 to 2008, he was European coordinator of FP6 Receptronics in the Nanotechnology thematic area. Since 2008, he has been coordinator of the Working Group on Energy Autonomous Systems within the European CATRENE initiative. Since 2014, he is member of the scientific board and team leader of the joint STMicroelectronics and Bologna University lab for sensor design. He has coauthored more than 100 publications, 18 granted U.S. patents and 11 European and WIPO patents. Prof. Tartagni was a co-recipient of the 2004 Jan Van Vessem Award of the IEEE International Solid-State Circuits Conference.